Tuning layer-hybridized moiré excitons by the quantum-confined Stark effect

Yanhao Tang[1], Jie Gu[1], Song Liu[2], Kenji Watanabe[3], Takashi Taniguchi[3], James Hone[2], Kin Fai Mak[1,4,5]*, Jie Shan[1,4,5]*

[1]School of Applied and Engineering Physics, Cornell University, Ithaca, NY, USA
[2]Department of Mechanical Engineering, Columbia University, New York, NY, USA
[3]National Institute for Materials Science, 1-1 Namiki, 305-0044 Tsukuba, Japan
[4]Laboratory of Atomic and Solid State Physics, Cornell University, Ithaca, NY, USA
[5]Kavli Institute at Cornell for Nanoscale Science, Ithaca, NY, USA
*Email: kinfai.mak@cornell.edu; jie.shan@cornell.edu

Moiré superlattices open an unprecedented opportunity for tailoring interactions between quantum particles [1–11] and their coupling to the electromagnetic fields [12–18]. Strong superlattice potential generates moiré minibands of excitons [16–18] -- bound pairs of electrons and holes that reside either in a single layer (intralayer excitons) or two separate layers (interlayer excitons). The twist-angle-controlled interlayer electronic hybridization can also mix the two types of excitons to combine their strengths [13,19,20]. Here, we report a direct observation of layer-hybridized moiré excitons in angle-aligned WSe_2/WS_2 and $MoSe_2/WS_2$ superlattices by optical reflectance spectroscopy. These excitons manifest a hallmark signature of strong coupling in WSe_2/WS_2, that is, energy level anticrossing and oscillator strength redistribution under a vertical electric field. They also exhibit doping-dependent renormalization and hybridization that are sensitive to the electronic correlation effects. Our findings have significant implications for emerging manybody states in two-dimensional semiconductors, such as exciton condensates [21] and Bose-Hubbard models [22], and optoelectronic applications of these materials.

One sentence summary: Optical spectroscopy provides a direct observation of layer-hybridized moiré excitons in angle-aligned TMD heterostructures.

Interlayer excitons in two-dimensional (2D) semiconductor heterostructures possess an out-of-plane electric dipole, enabling electric-field tuning of exciton resonance energies by the quantum-confined Stark effect [23–26]. The long lifetime of interlayer excitons also facilitates long-range exciton transport [27,28] and population buildup for exciton condensation [21]. However, unlike (bright) intralayer excitons that interact strongly with light [29], interlayer excitons, being spatially indirect, have negligible oscillator strength. This significantly limits their fundamental studies and applications. To gain oscillator strength, interlayer excitons can be mixed with intralayer excitons through interlayer hybridization of electrons or holes. Layer-hybridized excitons have been intensively searched in semiconductor heterostructures [30]. Recent experiments on 2D transition metal dichalcogenide (TMD) moiré superlattices have attributed new spectral features observed in reflectance contrast to layer-hybridized excitons [13,19,20,31,32]. The moiré superlattice potential provides extra Bragg reflection for quasi-momentum conservation and opens new optical transition paths to facilitate hybridization between intralayer and interlayer excitons. While these studies show the twist-angle-dependent exciton band structure,

direct evidence of layer-hybridized excitons and their continuous tuning, particularly in the presence of strong moiré potential, remain elusive.

Here we report a direct observation of layer-hybridized moiré excitons in angle-aligned WSe_2/WS_2 and $MoSe_2/WS_2$ heterobilayers. These excitons exhibit the characteristics of both an interlayer exciton (large out-of-plane electric dipole) and an intralayer exciton (appreciable oscillator strength). They are formed via spin-conserving resonant tunneling of electrons or holes between the layers. In particular, we observe strong exciton coupling with the hallmark signature of energy level anticrossing under an out-of-plane electric field in WSe_2/WS_2 heterobilayers. The coupling in $MoSe_2/WS_2$ heterobilayers is substantially weaker, but multiple layer-hybridized moiré excitons with distinct electric dipoles are discernable. We also observe strongly modified electron-exciton interactions in the presence of strong moiré potential and identify the correlation effects in the characteristics of layer-hybridized moiré excitons around half filling of the first electron moiré miniband in WSe_2/WS_2.

Monolayer TMD semiconductors possess a direct energy gap at the K and K' valleys of the Brillouin zone [29] (Fig. 1b, c). At these valleys the large spin-orbit coupling pins the electron spin in the out-of-plane direction and spin splits the bands. The splitting is ~ 10's and 100's meV at the conduction and valence band edges, respectively. The degenerate states at the two valleys have opposite spin alignments so that the time-reversal symmetry is preserved. We choose heterobilayers of WSe_2/WS_2 and $MoSe_2/WS_2$, in which closely aligned bands are present to enhance interlayer tunneling (see Methods for the determination of band alignments). The moiré lattice constant in angle-aligned heterobilayers of both types is about 8 nm [12,13].

We fabricate TMD heterobilayers by stacking two monolayers with a controlled twist angle between their crystal lattices. The misalignment is typically less than 0.5° (from 0° or 60°) in the angle-aligned samples. We employ a dual-gate device (Fig. 1a) to apply vertical electric field E_{appl} and doping to the heterobilayers independently. With two nearly symmetric gates as employed in this study, we introduce doping (but no field) by applying equal gate voltages of the same sign, and electric field (but no doping), by applying equal gate voltages of opposite sign. (See Methods for device fabrication and calibration of the doping level and electric field.) Multiple devices have been studied and consistent results have been observed in all devices of the same type.

The WSe_2/WS_2 heterobilayers have a type-II band alignment [3,11] (Fig. 1b, c). The lower valence band of WSe_2 is closely aligned with the upper valence band of WS_2. The lowest-energy layer-hybridized excitons (dashed double-arrowed line), if present, are expected to occur near the fundamental exciton resonance of WS_2 (solid double-arrowed line). We therefore focus on the spectrum around the fundamental exciton in WS_2 (~ 2 eV). A more complete dataset is shown in Extended Data Fig. 1. Figure 1d - f are the reflectance contrast spectra R of WSe_2/WS_2 heterobilayers with twist angles close to 20°, 60° and 0°, respectively, as a function of gate voltage V_G. The voltage is applied symmetrically to two gates, i.e. varying the doping density while E_{appl} = 0 V/nm. The three horizontal dashed lines correspond to filling factor ν = 0, 1 and 2, where ν = 1 corresponds to one

electron per moiré superlattice cell or half filling of the first electron moiré miniband located in the WS_2 layer.

Our result is consistent with recent reports [3,12]. With doping, the WS_2 fundamental A exciton weakens and a red-shifted charged exciton feature emerges. No clear B exciton can be identified presumably due to the large spectral linewidth. Effects of the moiré superlattice are observed only in angle-aligned samples (0° and 60°). They manifest as multiple minibands of intralayer excitons, which exhibit semi-periodic modulations with doping density. We label the two brightest ones X_1 and X_2. In particular, the fundamental intralayer moiré exciton X_1 carries the largest oscillator strength. We also observe a new spectral feature (iX) slightly below X_1 in the 60° sample, but not the 0° sample.

We examine the exciton response to an out-of-plane electric field to understand the origin of the new feature iX. Figure 2a-c shows the result for the 60° sample with ν fixed around 0, 1 and 2, respectively. We show the derivative of R with respect to photon energy to enhance the contrast of weak features. Line cuts of Fig. 2a-c at representative fields are included in Extended Data Fig. 2. The resonance features iX, X_1 and X_2 are all field dependent. When iX is far from X_1 and X_2, it disperses linearly with field and has small oscillator strength. In this regime, X_1 and X_2 show little dispersion with field. When iX approaches X_1 and X_2, energy level anticrossing is observed and iX rapidly gains oscillator strength. In sharp contrast, no discernible electric-field dependence is observed for moiré excitons in the 0° sample (Extended Data Fig. 3). This is expected since intralayer excitons do not have out-of-plane electric dipoles.

The linear out-of-plane electric-field response and negligible oscillator strength of iX when it is decoupled from other excitons support that iX is an interlayer exciton [23–25]. It arises from transitions from the lower valence band of WSe_2 to the conduction band of the same spin in WS_2 (Fig. 1b). Energy level anticrossing and oscillator strength redistribution between the interlayer and intralayer excitons signify their strong coupling. The phenomenon is observed only in samples with a twist angle close to 60°. In this configuration, extra Bragg reflection from the superlattice potential helps to conserve quasi-momentum and facilitate strong coupling. The closely aligned valance bands in the two layers have the same spin, which enables resonant hole tunneling when the bands are tuned into resonance by the electric field. This is not allowed in the 0° sample (Fig. 1c) since resonant tunneling is spin-forbidden and no layer-hybridized excitons are observed. We thus conclude that the layer-hybridized excitons are formed through spin-preserving resonant tunneling of holes between the layers in WSe_2/WS_2 moiré superlattices.

We model the coupled exciton system using a three-level Hamiltonian $\begin{pmatrix} \mathcal{E}_{\mathrm{iX}} & W_1 & W_2 \\ W_1^* & \mathcal{E}_1 & 0 \\ W_2^* & 0 & \mathcal{E}_2 \end{pmatrix}$. The diagonal elements describe the energy of uncoupled interlayer exciton $\mathcal{E}_{\mathrm{iX}}$ and two intralayer moiré excitons $\mathcal{E}_1$ and $\mathcal{E}_2$ ($> \mathcal{E}_1$). Although multiple iXs are present, only one is observed to couple strongly with the intralayer excitons in this system. The interlayer exciton energy is linear in electric field, $\mathcal{E}_{\mathrm{iX}} = \mathcal{E}_0 + DE_{appl}$, where $\mathcal{E}_0$ is the energy at zero field and D is the effective out-of-plane electric dipole. The intralayer exciton energies

are field independent. The off-diagonal element W_j and its complex conjugate W_j^* are the coupling constant between the interlayer exciton and intralayer moiré exciton X_j (j = 1, 2). We assume the intralayer moiré excitons do not couple between themselves for simplicity.

The black dashed lines in Fig. 2 are the best fit of the experimental data to the three-level model. In Fig. 2d-f we show a detailed comparison between the field-dependent exciton energies from the experiment (solid lines) and the model with coupling (dashed lines) and without coupling (dotted lines). Comparison for the exciton oscillator strength is provided in Extended Data Fig. 4. The agreement between experiment and model is generally excellent. The extracted coupling constants $|W_1| \approx 40$ meV and $|W_2| \approx 30$ meV exceed the exciton linewidths (≈ 10 meV). The system is thus in the strong coupling regime. The large coupling constants are an indication of strong moiré potential since both are related to the interlayer electronic tunneling rate. The extracted values of $|W_1|$ and $|W_2|$ are comparable to the moiré potential amplitude inferred from the intralayer moiré exciton spectrum (~ 25 meV) [12]. The extracted effective electric dipole $D \approx 0.35 - 0.4$ $e \cdot$nm (e denoting the elementary charge) is also consistent with the estimate from electrostatics $D \approx \frac{\epsilon_{hBN}}{\epsilon_W} et \approx 0.3$ e·nm (see Methods). We have used layer separation $t \approx$ 0.7 nm, $\epsilon_{hBN} \approx 3$ and $\epsilon_W \approx 7$ for the out-of-plane dielectric constant of hBN and TMDs, respectively.

Layer-hybridized moiré excitons are also observed in angle-aligned $MoSe_2/WS_2$ heterobilayers. Here the conduction bands of the two layers can be brought into resonance for resonant tunneling (Fig. 3a). The fundamental intralayer exciton in $MoSe_2$ (solid double-arrowed line) and the fundamental interlayer exciton (dashed double-arrowed line) hybridize. In contrast to WSe_2/WS_2, the coupling is substantially weaker and level anticrossing under an out-of-plane field is not clearly resolved (Fig. 3b). In particular, hybridization is not observed for the fundamental intralayer moiré exciton (X_1) although it was thought to be a layer-hybridized exciton [13,18]. Multiple layer-hybridized moiré excitons can be discerned with two distinct electric-field dispersions. We refer to the family of interlayer excitons that hybridize with the second (third) intralayer moiré exciton X_2 (X_3) as iX_2 (iX_3) originating from transitions to higher-energy moiré bands [18]. Similar behavior is observed for second device in Extended Data Fig. 5.

The best fit of the experimental data to a two-level model yields D ~ 0.24 and 0.17 e·nm for iX_2 and iX_3, respectively (Fig. 3c). The difference likely arises from localization of the exciton center-of-mass wavefunction (Bohr radius of ~ 2 nm [18] is much smaller than the moiré superlattice constant) at different sites of the moiré superlattice cell formed by overlaying two incommensurate crystal lattices. This is known for intralayer moiré excitons [12,17]. Spatially varying dielectric function (potentially also layer separation from atomic reconstruction) could account for the difference in D for iX_2 and iX_3. This could also explain the difference in D between $MoSe_2/WS_2$ and WSe_2/WS_2 although their average layer separation is similar. The extracted coupling constants for the iX_2- and iX_3-families are ~ 1 and 3 meV, respectively. They are smaller than the exciton linewidths (~ 5-10 meV) and the system is not in the strong coupling regime. For efficient control and manipulation of interlayer-hybridized excitons, future studies are required to identify

systems in the strong coupling regime for the fundamental excitons (as demonstrated above for high-energy excitons in WSe_2/WS_2).
Finally we examine the doping effect on layer-hybridized excitons in the strong coupling regime. Figure 1e already shows that the presence of strong moiré potential in WSe_2/WS_2 significantly modifies the behavior of electron-exciton interactions. The exciton energy and oscillator strength are no longer a continuous function of doping density while filling the first electron moiré miniband ($0 < \nu < 2$). Similar behavior is observed under fixed electric fields (Extended Data Fig. 6). We measure the electric-field dependence of the exciton energies at each fixed electron density and compare it to the three-level model (examples are given in Fig. 2). Figure 4 summarizes the fitting parameters as a function of ν (top axis) and gate voltage (bottom axis). For a considerable range of ν away from the integers, two spectral features are discernable for hybridized X_1. We have included both in the analysis (Extended Data Fig. 7) and used the size of the symbols to represent their strength in Fig. 4.

Figure 4a illustrates the doping-dependent energy of the uncoupled intralayer excitons ($\mathcal{E}_1$ and $\mathcal{E}_2$) and interlayer exciton at zero field ($\mathcal{E}_0$). Figure 4b and 4c are the doping dependence of the coupling constants and the effective dipole moment, respectively. The result shows that the properties of layer-hybridized excitons can be effectively tuned by doping. Most strikingly, $\mathcal{E}_0$ and $\mathcal{E}_1$ can be tuned by as much as 40 and 60 meV, respectively, with opposite slopes. At each integer filling, there is only one branch of X_1. When the system is doped away from it on either side, the intensity decreases gradually but the energy stays nearly unchanged. Meanwhile, a new branch emerges at a different energy, grows in strength, and eventually takes over the optical response. The doping dependence of $\mathcal{E}_0$ follows closely that of the stronger branch of $\mathcal{E}_1$.

The maximum oscillator strength of the excitons at integer fillings (ν = 0, 1 and 2) is a manifestation of the gapped nature of these states since the Coulomb gap suppresses free carrier screening of the exciton interactions. Unlike ν = 0 and 2 which correspond to single-particle band gaps, the ν = 1 state (half-filled band) is driven by interactions. Recent studies show that it is a Mott insulating state with a large Coulomb gap between the lower and upper Hubbard bands [3,11]. The plateau-like behavior of the exciton energies is not understood. It could be related to the localized exciton wavefunction in the moiré superlattice, which makes excitons behave as 'quantum confined'. The idea of localized exciton and electron wavefunctions could also be invoked to explain the observed doping dependence of the coupling constants through exciton wavefunction overlap [18] (Fig. 4b) and the effective electric dipole through the local TMD dielectric function (Fig. 4c). The optical properties of a doped moiré superlattice with strong moiré potential are extremely complex and rich. The system provides an exciting platform to understand, explore, and manipulate the layer-hybridized moiré excitons and their interplay with emerging correlated states.

References

1. Cao, Y. *et al.* Correlated insulator behaviour at half-filling in magic-angle graphene superlattices. *Nature* **556**, 80–84 (2018).

2. Cao, Y. *et al.* Unconventional superconductivity in magic-angle graphene superlattices. *Nature* **556**, 43–50 (2018).
3. Tang, Y. *et al.* Simulation of Hubbard model physics in WSe_2/WS_2 moiré superlattices. *Nature* **579**, 353–358 (2020).
4. Serlin, M. *et al.* Intrinsic quantized anomalous Hall effect in a moiré heterostructure. *Science* **367**, 900–903 (2020).
5. Chen, G. *et al.* Evidence of a gate-tunable Mott insulator in a trilayer graphene moiré superlattice. *Nat. Phys.* **15**, 237–241 (2019).
6. Chen, G. *et al.* Tunable correlated Chern insulator and ferromagnetism in a moiré superlattice. *Nature* **579**, 56–61 (2020).
7. Lu, X. *et al.* Superconductors, orbital magnets and correlated states in magic-angle bilayer graphene. *Nature* **574**, 653–657 (2019).
8. Chen, G. *et al.* Signatures of tunable superconductivity in a trilayer graphene moiré superlattice. *Nature* **572**, 215–219 (2019).
9. Yankowitz, M. *et al.* Tuning superconductivity in twisted bilayer graphene. *Science* **363**, 1059–1064 (2019).
10. Sharpe, A. L. *et al.* Emergent ferromagnetism near three-quarters filling in twisted bilayer graphene. *Science* **365**, 605–608 (2019).
11. Regan, E. C. *et al.* Mott and generalized Wigner crystal states in WSe_2/WS_2 moiré superlattices. *Nature* **579**, 359–363 (2020).
12. Jin, C. *et al.* Observation of moiré excitons in WSe_2/WS_2 heterostructure superlattices. *Nature* **567**, 76–80 (2019).
13. Alexeev, E. M. *et al.* Resonantly hybridized excitons in moiré superlattices in van der Waals heterostructures. *Nature* **567**, 81–86 (2019).
14. Tran, K. *et al.* Evidence for moiré excitons in van der Waals heterostructures. *Nature* **567**, 71–75 (2019).
15. Seyler, K. L. *et al.* Signatures of moiré-trapped valley excitons in $MoSe_2/WSe_2$ heterobilayers. *Nature* **567**, 66–70 (2019).
16. Wu, F., Lovorn, T. & MacDonald, A. H. Topological Exciton Bands in Moiré Heterojunctions. *Phys. Rev. Lett.* **118**, 147401 (2017).
17. Yu, H., Liu, G.-B., Tang, J., Xu, X. & Yao, W. Moiré excitons: From programmable quantum emitter arrays to spin-orbit–coupled artificial lattices. *Sci. Adv.* **3**, e1701696 (2017).
18. Ruiz-Tijerina, D. A. & Fal'Ko, V. I. Interlayer hybridization and moiré superlattice minibands for electrons and excitons in heterobilayers of transition-metal dichalcogenides. *Phys. Rev. B* **99**, 30–32 (2019).
19. Shimazaki, Y. *et al.* Strongly correlated electrons and hybrid excitons in a moiré heterostructure. *Nature* **580**, 472–477 (2020).
20. Sung, J. *et al.* Broken mirror symmetry in excitonic response of reconstructed domains in twisted $MoSe_2/MoSe_2$ bilayers. *Nat. Nanotechnol.* **15**, 7–12 (2020).
21. Wang, Z. *et al.* Evidence of high-temperature exciton condensation in two-dimensional atomic double layers. *Nature* **574**, 76–80 (2019).
22. Capogrosso-Sansone, B., Prokof'ev, N. V & Svistunov, B. V. Phase diagram and thermodynamics of the three-dimensional Bose-Hubbard model. *Phys. Rev. B* **75**, 134302 (2007).
23. Wang, Z., Chiu, Y.-H., Honz, K., Mak, K. F. & Shan, J. Electrical Tuning of

Interlayer Exciton Gases in WSe_2 Bilayers. *Nano Lett.* **18**, 137–143 (2018).
24. Ciarrocchi, A. *et al.* Polarization switching and electrical control of interlayer excitons in two-dimensional van der Waals heterostructures. *Nat. Photonics* **13**, 131–136 (2019).
25. Jauregui, L. A. *et al.* Electrical control of interlayer exciton dynamics in atomically thin heterostructures. *Science* **366**, 870–875 (2019).
26. Rivera, P. *et al.* Interlayer valley excitons in heterobilayers of transition metal dichalcogenides. *Nat. Nanotechnol.* **13**, 1004–1015 (2018).
27. Unuchek, D. *et al.* Room-temperature electrical control of exciton flux in a van der Waals heterostructure. *Nature* **560**, 340–344 (2018).
28. Jin, C. *et al.* Imaging of pure spin-valley diffusion current in WS_2/WSe_2 heterostructures. *Science* **360**, 893–896 (2018).
29. Mak, K. F. & Shan, J. Photonics and optoelectronics of 2D semiconductor transition metal dichalcogenides. *Nat. Photonics* **10**, 216 (2016).
30. Cristofolini, P. *et al.* Coupling Quantum Tunneling with Cavity Photons. *Science* **336**, 704–707 (2012).
31. Zhang, L. *et al.* Moiré lattice-induced formation and tuning of hybrid dipolar excitons in twisted $WS_2/MoSe_2$ heterobilayers. *arXiv:1911.10069* (2019).
32. Hsu, W.-T. *et al.* Tailoring excitonic states of van der Waals bilayers through stacking configuration, band alignment, and valley spin. *Sci. Adv.* **5**, eaax7407 (2019).

Methods

Sample preparation and device fabrication

Dual-gated WSe_2/WS_2 and $MoSe_2/WS_2$ heterobilayers were employed for the optical measurements. The two nearly symmetric gates are made of hexagonal boron nitride (hBN) of ~ 20 nm in thickness and few-layer graphite. The heterobilayers are grounded through another piece of few-layer graphite. The devices were fabricated by the dry transfer method reported in the literature [3,33]. In short, atomically thin flakes were exfoliated from bulk crystals onto SiO_2/Si substrates and then stacked on top of each other. Angle alignment of the two TMD monolayers with precision of about 0.5° was assisted by angle-resolved optical second harmonic generation (SHG) measurements (Extended Data Fig. 8). Details of the SHG measurement have been reported by recent studies [3,12]. The SHG intensity from monolayer TMDs has a six-fold pattern, which correlates with the crystal axes and allows their alignment during the transfer. Furthermore, the SHG intensity from the heterobilayers is constructively enhanced and destructively suppressed for 0°- and 60°-samples, respectively, allowing us to distinguish these two cases.

Reflection contrast measurements

Details of the reflection contrast measurement have been reported in ref. [3]. In short, the white light output of a halogen lamp was collimated and focused onto the sample by an objective with a diffraction-limited spot. The reflected light was collected by the same objective and detected by a liquid-nitrogen cooled CCD camera coupled to a spectrometer. The reflectance contrast spectrum $R \equiv (I' - I)/I$ was obtained by

comparing the reflected light intensity from the sample (I') to a featureless spectrum (I) from the substrate. We have also taken the energy-derivative of the reflectance contrast spectrum numerically to enhance the spectral features in Fig. 2 and 3. The sample was grounded during the optical measurements, and the top and bottom gate voltages were controlled by two sourcemeters (Keithley 2400). The device was mounted in a closed-cycle cryostat with temperature of 5 K (Montana Instruments).

Calibration of doping density and electric field

The doping density in the TMD bilayers was determined from the applied gate voltages using a parallel-plate capacitor model, details of which have been reported [3]. To summarize, the doping density was calculated by the sum of the two applied gate voltages and the geometric capacitances of the nearly symmetric top and bottom gates. The geometric capacitance is determined by the thickness of the hBN dielectric (measured by atomic force microscopy) and its dielectric constant $\epsilon_{hBN} \approx 3$ [34]. The filling factor was then determined from the doping density and the calculated moiré density based on the known lattice constants and the twist angle. Whereas symmetric gating induces doping, antisymmetric gating applies an out-of-plane electric field to the sample. The electric field was calculated by the voltage difference applied to the two gates divided by the total thickness of the device measured by atomic force microscopy.

Electrostatic model for interlayer excitons in TMD bilayers

To obtain the effective out-of-plane electric dipole D of interlayer excitons in TMD heterobilayers, we calculate the local electric field E_{W} within the bilayer for a given applied field E_{appl}, using the parallel-plate capacitor model. Following ref. [23], we obtain for symmetric top and bottom gates,

$$E_W \approx \frac{\epsilon_{hBN}}{\epsilon_W} E_{appl}. \quad (1)$$

Here ϵ_W is the local effective out-of-plane dielectric constant for the TMD heterobilayer. For a fixed doping density n, the Stark shift $\mathcal{E}_{iX}$ for interlayer excitons becomes

$$\mathcal{E}_{iX} = et \cdot E_W \approx et \frac{\epsilon_{hBN}}{\epsilon_W} E_{appl} = DE_{appl}, \quad (2)$$

where $D \approx \frac{\epsilon_{hBN}}{\epsilon_W} et$ is the effective out-of-plane electric dipole and is dependent on the local dielectric environment of the moiré superlattice.

Band alignment in WSe_2/WS_2 and $MoSe_2/WS_2$ heterobilayers

We construct the band alignment in WSe_2/WS_2 by combining optical reflection and photoluminescence (PL) measurements. Extended Data Fig. 9 shows the constructed type-II band alignment for 60 °-aligned WSe_2/WS_2 bilayers. First, we obtain the fundamental interlayer optical gap from the interlayer exciton PL centered at ~ 1.43 eV (Extended Data Fig. 9b). It involves spin-preserved transitions between the lowest conduction band in WS_2 and the highest valence band in WSe_2. Second, the first intralayer moiré exciton transition in WS_2 is centered at ~ 2.01 eV in the absence of doping (Fig. 1e). It originates from the spin-preserved transitions between the highest

valance band and the spin-split conduction band in WS_2. Third, the valence band spin-splitting in WSe_2 is ~ 0.45 eV [35] and the conduction band spin-splitting in WS_2 is ~ 0.03 eV [36]. Combining these values, the band alignment can be obtained in Extended Data Fig. 9, which agrees well with the density functional theory result [37]. Since the interlayer exciton binding energy is slightly smaller than that of intralayer excitons, the true band alignment can deviate slightly from Extended Data Fig. 9. With finite doping, the band alignment is renormalized as suggested by the result in Fig. 4a.

Whereas WSe_2/WS_2 has a type-II band alignment, $MoSe_2/WS_2$ has a type-I band alignment. This was determined from the doping-dependent reflectance contrast measurement for angle-misaligned $MoSe_2/WS_2$ bilayer in Extended Data Fig. 10. Charged excitons are formed in the $MoSe_2$ layer upon both electron and hole doping. In contrast, positively (negatively) charged excitons are formed in the WSe_2 (WS_2) layer upon hole (electron) doping in WSe_2/WS_2 (Extended Data Fig. 1a,b).

Methods references

33. Wang, L. *et al.* One-dimensional electrical contact to a two-dimensional material. *Science.* **342**, 614–617 (2013).
34. Movva, H. C. P. *et al.* Density-Dependent Quantum Hall States and Zeeman Splitting in Monolayer and Bilayer WSe_2. *Phys. Rev. Lett.* **118**, 247701 (2017).
35. Li, Y. *et al.* Measurement of the optical dielectric function of monolayer transition-metal dichalcogenides: MoS_2, $MoSe_2$, WS_2, and WSe_2. *Phys. Rev. B* **90**, 205422 (2014).
36. Liu, G.-B., Shan, W.-Y., Yao, Y., Yao, W. & Xiao, D. Three-band tight-binding model for monolayers of group-VIB transition metal dichalcogenides. *Phys. Rev. B* **88**, 85433 (2013).
37. Kang, J., Tongay, S., Zhou, J., Li, J. & Wu, J. Band offsets and heterostructures of two-dimensional semiconductors. *Appl. Phys. Lett.* **102**, 12111 (2013).

Data availability

The data that support the findings of this study are available within the paper and its Supplementary Information. Additional data are available from the corresponding authors upon request.

Acknowledgements

Research was primarily supported by the US Department of Energy (DOE), Office of Science, Basic Energy Sciences (BES), under award number DE-SC0019481 (optical spectroscopy and growth of WSe_2 crystals). Device fabrication was supported by the Air Force Office of Scientific Research Hybrid Materials MURI under award number FA9550-18-1-0480, and analysis and modeling were supported by the U. S. Army Research Office under award number W911NF-17-1-0605 and the National Science Foundation under award number DMR-2004451. The growth of the hBN crystals was

supported by the Elemental Strategy Initiative of MEXT, Japan and CREST (JPMJCR15F3), Japan Science and Technology Agency.

Author contributions

Y.T. and J. G. fabricated the devices and performed the optical measurements; S.L. and J.H. grew the bulk TMD crystals; K.W. and T.T. grew the bulk hBN crystals. Y.T., K.F.M. and J.S. designed the study, performed the analysis and co-wrote the manuscript. All authors discussed the results and commented on the manuscript.

Competing interests

The authors declare no competing interests.

Author information

Supplementary information is available in the online version of the paper.
Reprints and permission information is available online at www.nature.com/reprints.
Correspondence and requests for materials should be addressed to K.F.M. or J.S.

Figure captions

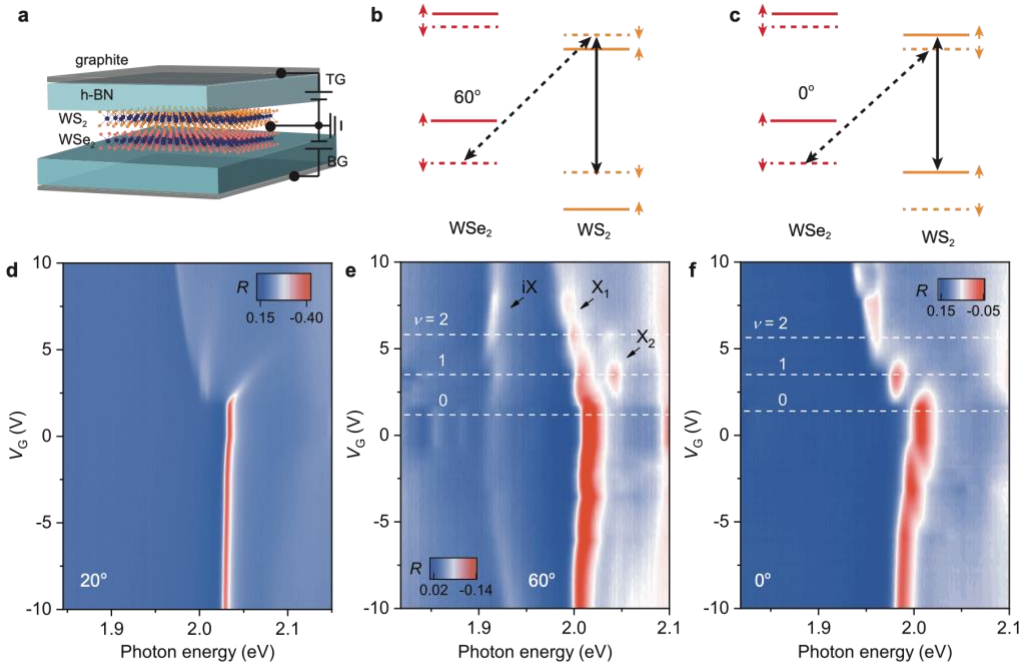

Figure 1 | Doping-dependent reflectance contrast spectrum of WSe_2/WS_2 bilayers. **a,** Schematic dual-gate device structure. The WSe_2/WS_2 bilayer is encapsulated by nearly symmetric top and bottom gates made of hBN and few-layer graphite. **b, c,** Type-II band alignment for near-60°- (**b**) and 0°- (**c**) aligned samples. Spin-up (spin-down) bands are denoted by solid (dotted) lines. Solid (dashed) double-sided arrows denote intralayer (interlayer) dipole-allowed optical transitions. Mixing of the two types of transitions is allowed only in the near-60°-aligned samples. **d**, **e, f,** Contour plot of the gate-dependent reflectance contrast spectrum for ~ 20° (**d**), ~ 60° (**e**) and ~ 0° (**f**) samples. Gate voltage is applied symmetrically on both gates. The white dashed lines denote the gate voltage for filling factor ν = 0, 1 and 2 (ν = 2 corresponds to full filling of the first moiré conduction band of the WS_2 layer). The spectral features in **e** are assigned interlayer, first and second intralayer moiré excitons, iX, X_1 and X_2, respectively.

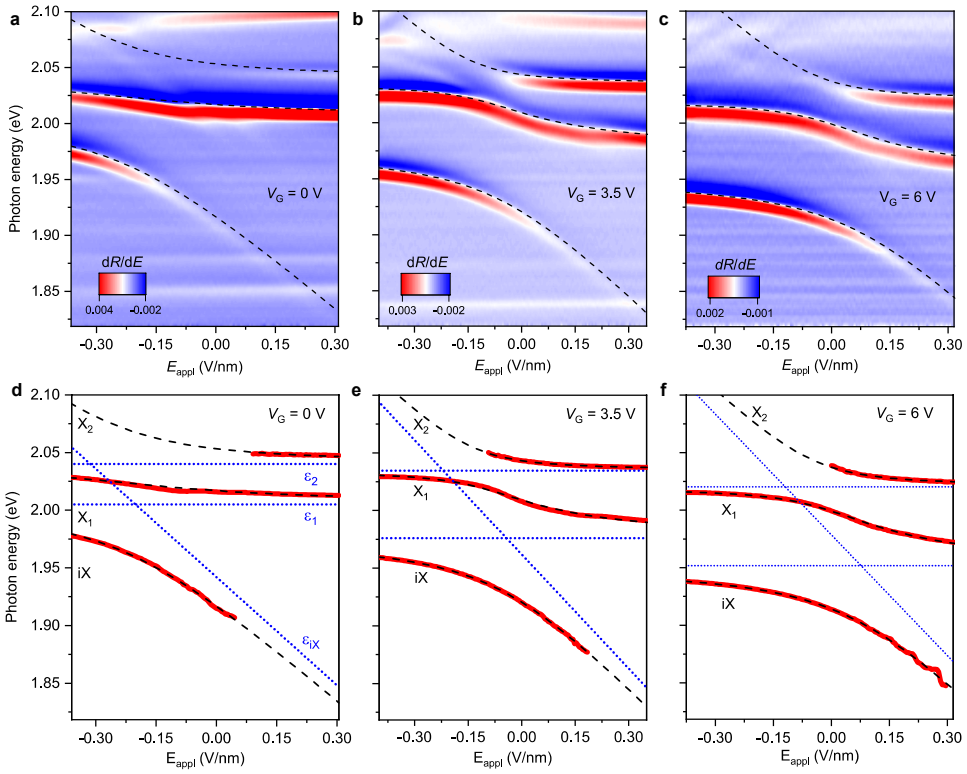

Figure 2 | Electric-field dependence of layer-hybridized excitons in WSe_2/WS_2 moiré superlattice. **a**, **b, c,** Energy-derivative of the reflectance contrast spectrum as a function of applied out-of-plane electric field in 60°-aligned sample at a fixed doping density near ν = 0 (**a**), 1 (**b**) and 2 (**c**). The dashed lines are the best fit to the three-level model described in the text. **d**, **e, f,** Electric-field dependence of the exciton resonance energies extracted from **a**, **b, c** correspondingly. Solid red lines and dashed black lines represent experimental data and the best-fit three-level model, respectively. The dotted lines show the dispersion for uncoupled exciton states.

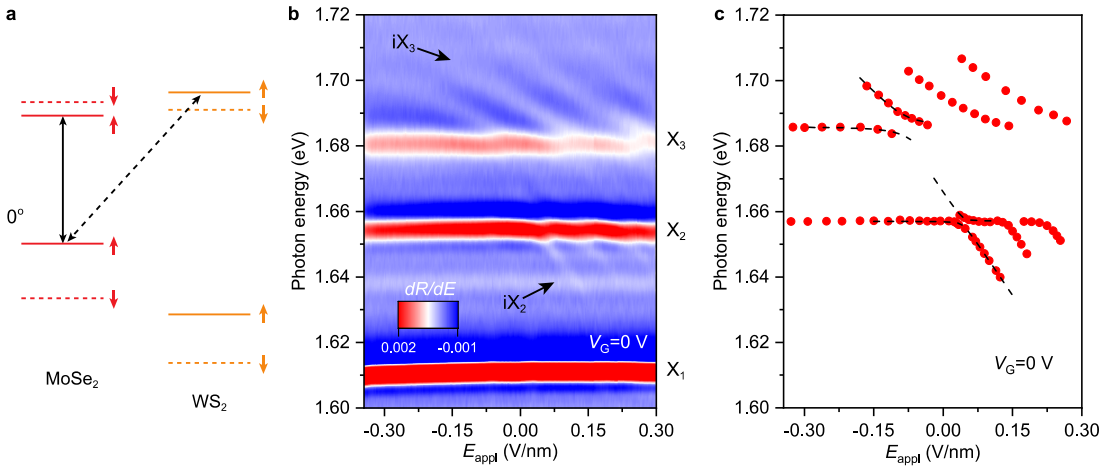

Figure 3 | Electric-field dependence of layer-hybridized excitons in $MoSe_2/WS_2$ moiré superlattice. **a,** Type-I band alignment for ~ 0°-aligned samples. Mixing of intralayer and interlayer excitons is allowed for both ~ 0° and ~ 60° samples because of the small spin-splitting of the conduction bands. **b,** Energy-derivative of the reflectance contrast spectrum as a function of electric field in the absence of doping. X_1, X_2 and X_3 denote the first three intralayer moiré excitons; iX_2 and iX_3 denote the family of interlayer excitons that hybridize with X_2 and X_3, respectively. **c,** Electric-field dependence of the exciton resonance energies extracted from **b** (symbols). Dashed lines are fits to a two-level model.

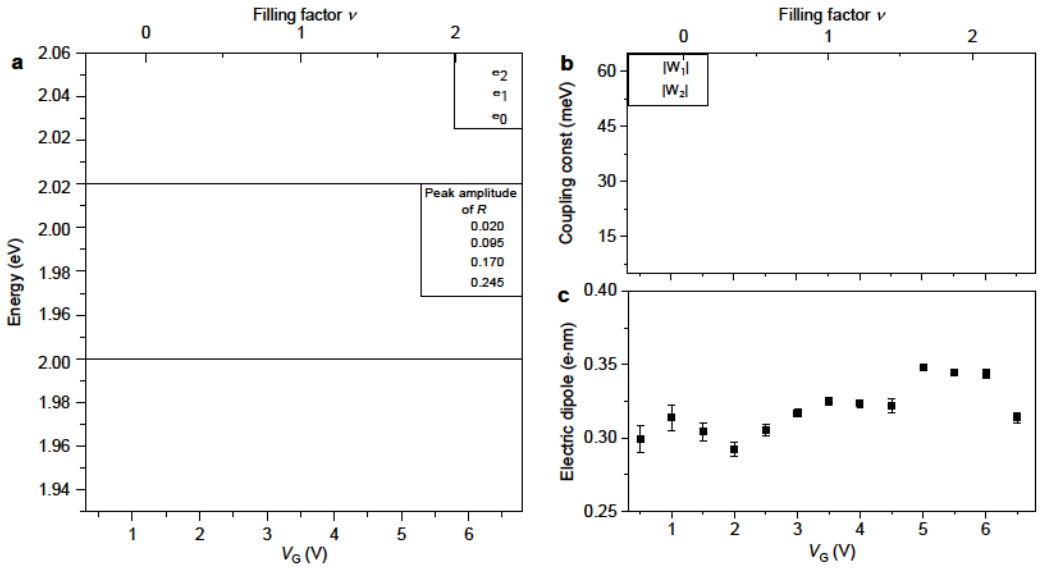

Figure 4 | Doping dependence of layer-hybridized excitons in WSe_2/WS_2 moiré superlattice. a, Uncoupled intralayer and interlayer exciton resonance energies at zero electric field as a function of gate voltage (bottom axis) and filling factor (top axis). **b**, **c**, Doping dependence of exciton coupling constants (**b**) and interlayer exciton effective out-of-plane electric dipole (**c**). The size of the symbols in **a** (middle panel) and **b** represents the oscillator strength of the two spectral features of X_1. The error bars represent the fitting uncertainties to the three-level model.

Extended Data Figure captions

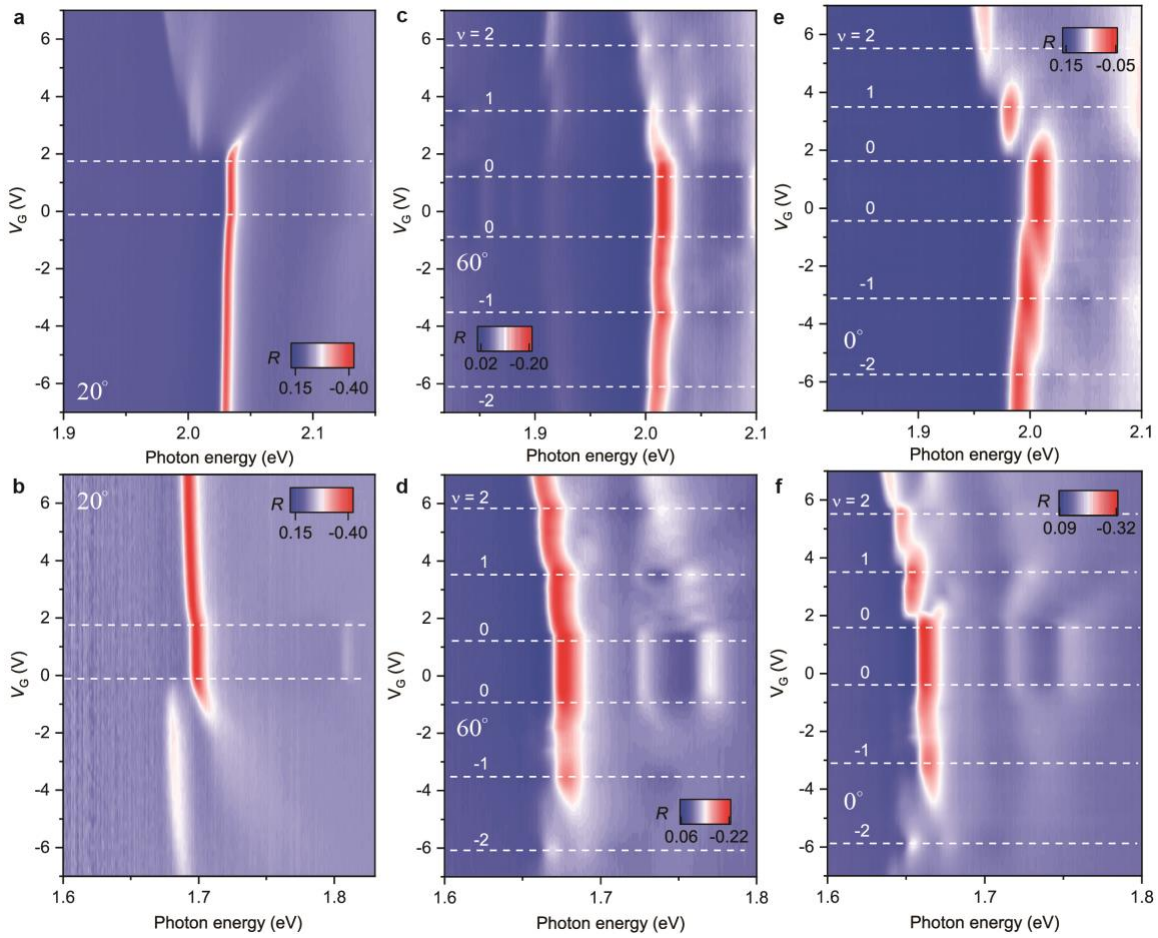

Extended Data Figure 1 | Doping-dependent reflectance contrast in WSe_2/WS_2 bilayers. Results are from WSe_2/WS_2 bilayers with a twist angle close to 20° (**a,b**), 60° (**c,d**), and 0° (**e,f**). Upper and lower panels show the energy windows corresponding to the fundamental exciton resonances in WS_2 and WSe_2, respectively. The horizontal dashed lines denote the filling factors of the moiré superlattice ($\boldsymbol{\nu} > 0$ for electron filling and $\boldsymbol{\nu} < 0$ for hole filling).

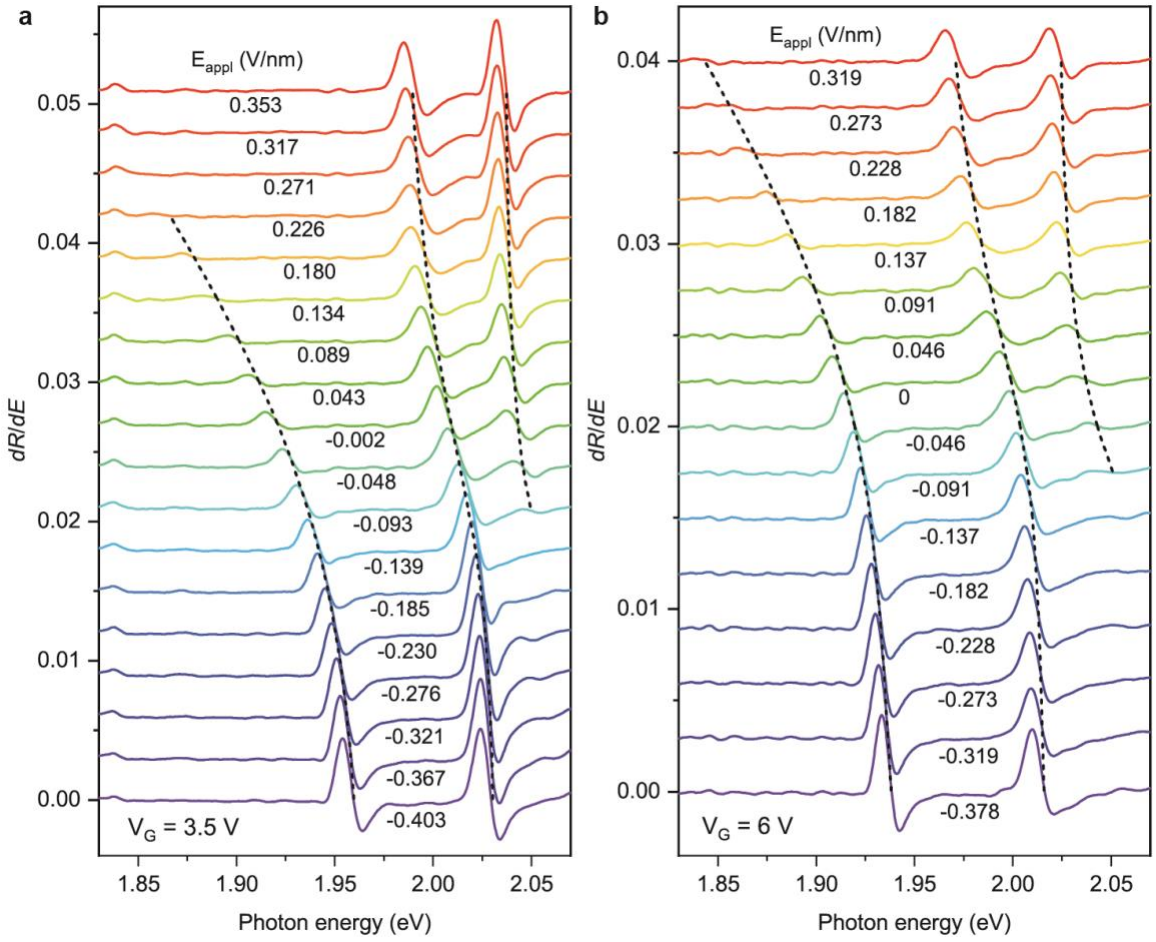

Extended Data Figure 2 | Electric-field dependence of layer-hybridized excitons in 60°-aligned WSe_2/WS_2 moiré superlattice. Energy derivative of the reflectance contrast spectrum at selected electric fields is shown for gate voltage at 3.5 V (**a**) and 6 V (**b**) (corresponding to filling factor close to 1 and 2). The spectra are vertically displaced for clarity. The dotted lines are guides to the eye for the resonance energy of the exciton features.

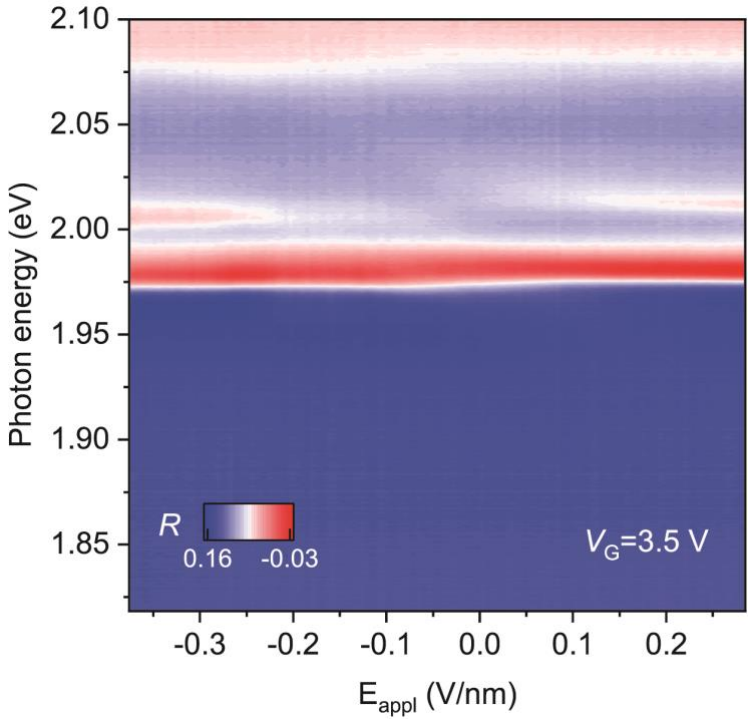

Extended Data Figure 3 | Electric-field dependence of excitons in 0°-aligned WSe_2/WS_2. Contour plot of the reflectance contrast spectrum as a function of applied electric field at fixed filling factor near 1. Interlayer excitons are not observed. The intralayer exciton resonances do not depend on the electric field.

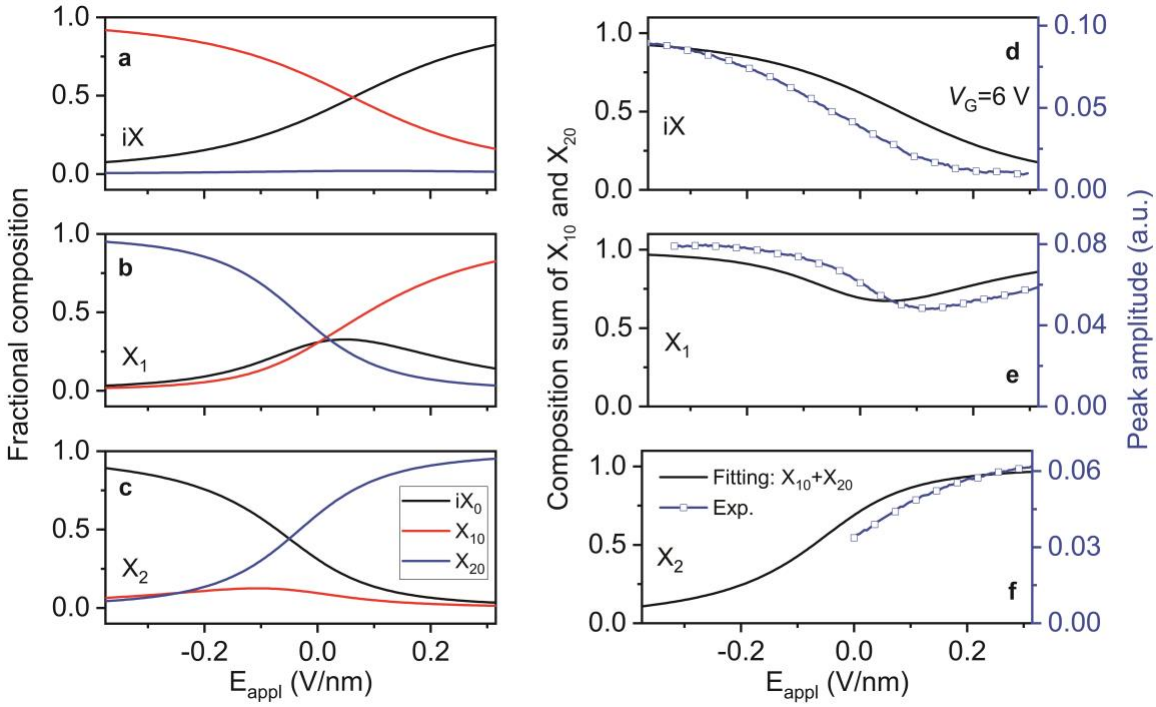

Extended Data Figure 4 | Electric-field dependence of hybridized exciton amplitudes. **a**, **b, c,** Decomposition of the amplitude squared of the hybridized iX (**a**), X_1 (**b**) and X_2 (**c**) states into the uncoupled states at varying electric fields. Black, red and blue lines denote the amplitude squared of the uncoupled interlayer exciton iX_0, intralayer exciton X_{10} and intralayer exciton X_{20} states, respectively. The results are obtained by solving the eigenvalue equation for the three-level system described in the main text. All of the states in the three-level Hamiltonian are normalized. **d**, **e, f,** Electric-field dependence of the sum of the uncoupled X_{10} and X_{20} amplitude squared (solid line) for the hybridized iX (**d**), X_1 (**e**) and X_2 (**f**) states. The calculated results are compared to the peak amplitude (proportional to oscillator strength) of the corresponding excitons (symbols connected by blue lines). Since only the uncoupled intralayer excitons X_{10} and X_{20} couple to light strongly, the oscillator strength of the hybridized excitons is well approximated by the sum of these two contributions. The experimental results agree reasonably well with the three-level model.

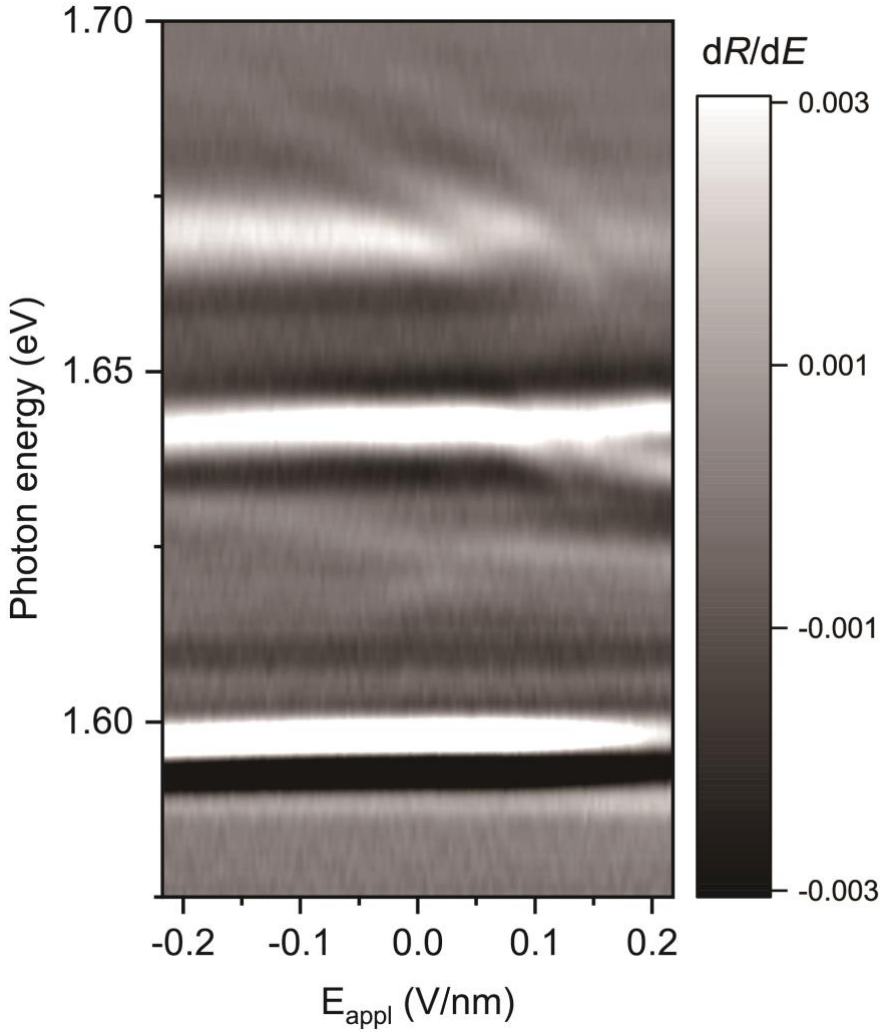

Extended Data Figure 5 | Electric-field dependence of layer-hybridized excitons in $MoSe_2/WS_2$ moiré superlattice (second device).

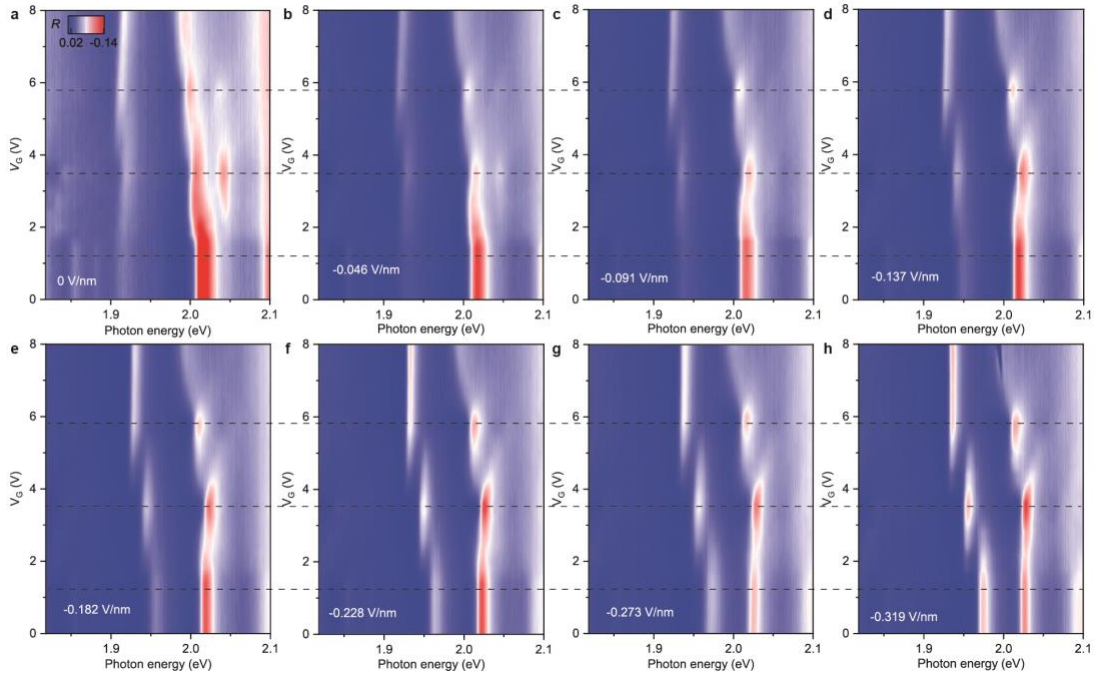

Extended Data Figure 6 | Doping dependence of layer-hybridized excitons in 60°-aligned WSe_2/WS_2 moiré superlattice under fixed electric fields (a –h). The dashed lines denote from bottom to top filling factor 0, 1, and 2.

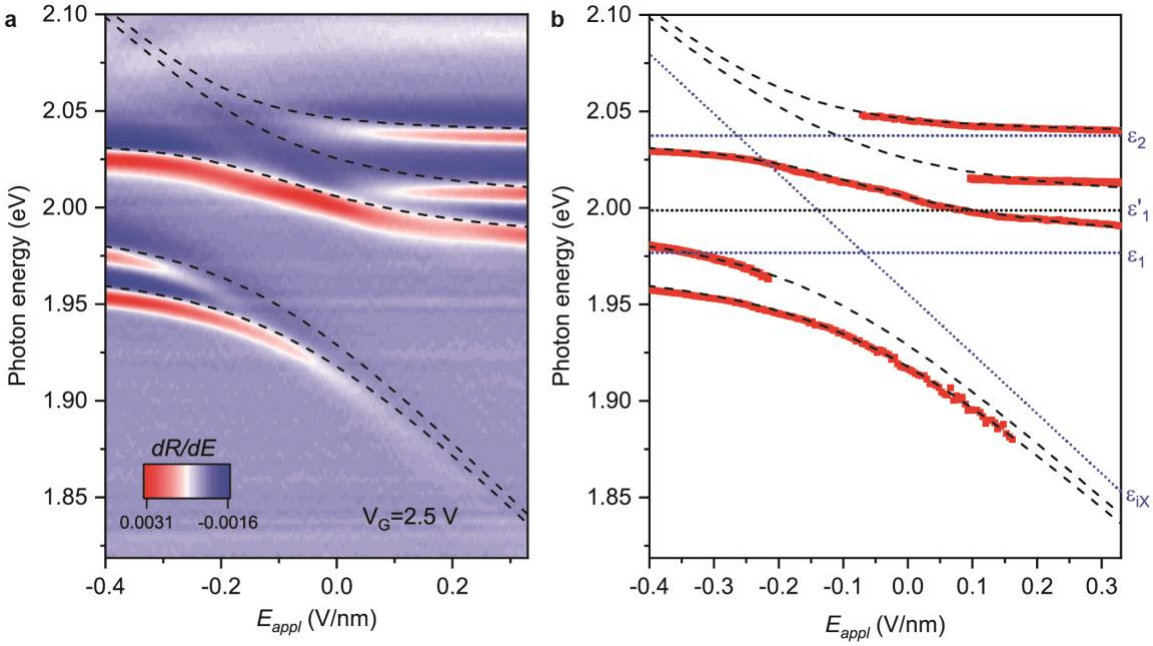

Extended Data Figure 7 | Electric-field dependence of layer-hybridized excitons in WSe_2/WS_2 moiré superlattice at filling factor of 0.57 (V_G=2.5 V). Same measurement as in Fig. 2 away from integer filling factors. Two spectral features are discernable for

hybridized X1. Coupled three-level analysis is performed for each feature. The extracted parameters from the model are shown in Fig. 4 with the size of the symbols representing the oscillator strength of the two features.

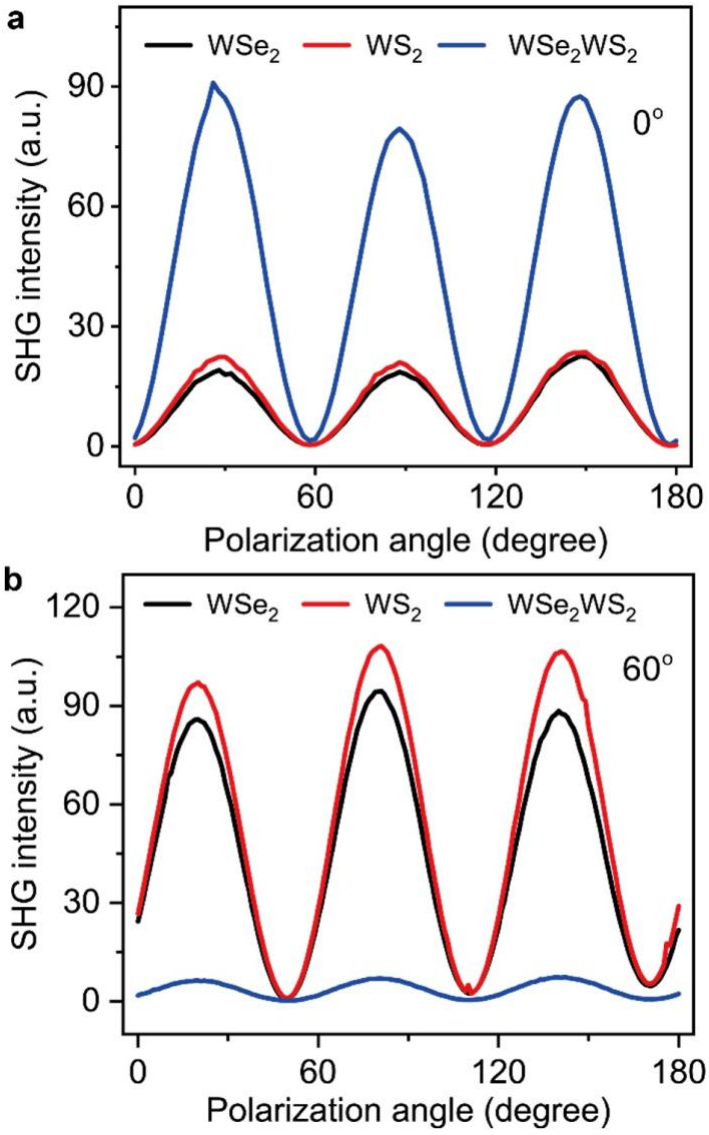

Extended Data Figure 8 | Polarization-resolved SHG intensity. **a, b,** Second-harmonic intensity as a function of the polarization angle of the excitation light from WSe_2/WS_2 bilayers with a twist angle close to 0° (**a**) and 60° (**b**). Black, red and blue lines represent measurements on the isolated WSe_2 monolayer, isolated WS_2 monolayer, and bilayer, respectively. Samples are excited by linearly polarized light under normal incidence. The cross-polarized component of the second harmonic is detected. The second-harmonic radiation from each monolayer is added constructively in the 0° bilayer sample (**a**) and destructively in the 60° bilayer sample (**b**).

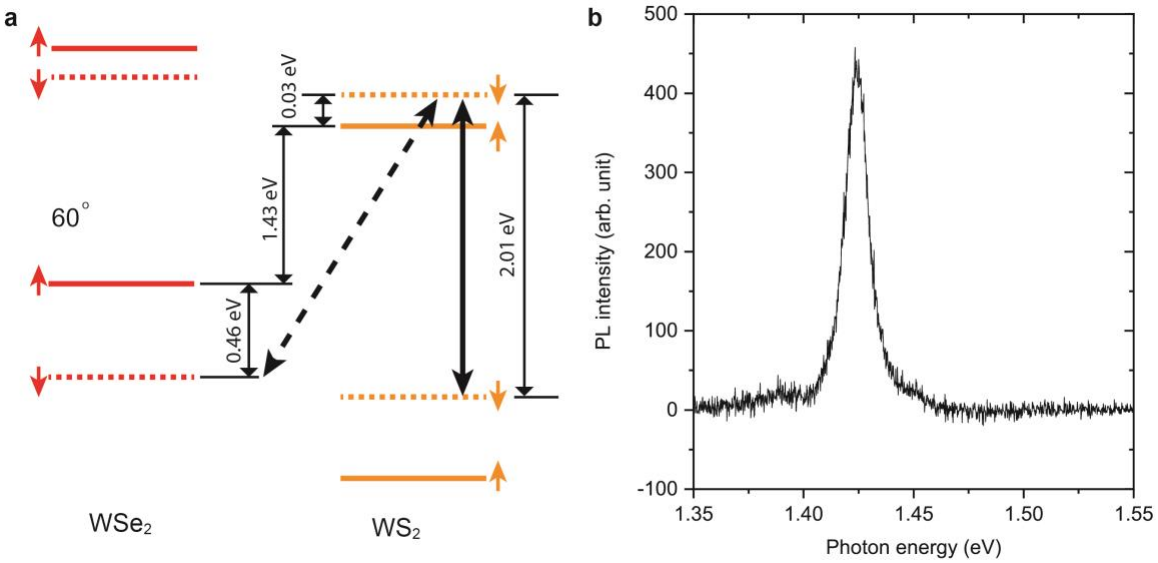

Extended Data Figure 9 | Band alignment in WSe_2/WS_2. Type-II band alignment of 60°-aligned WSe_2/WS_2 bilayer (**a**) and PL spectrum of the fundamental interlayer exciton (**b**).

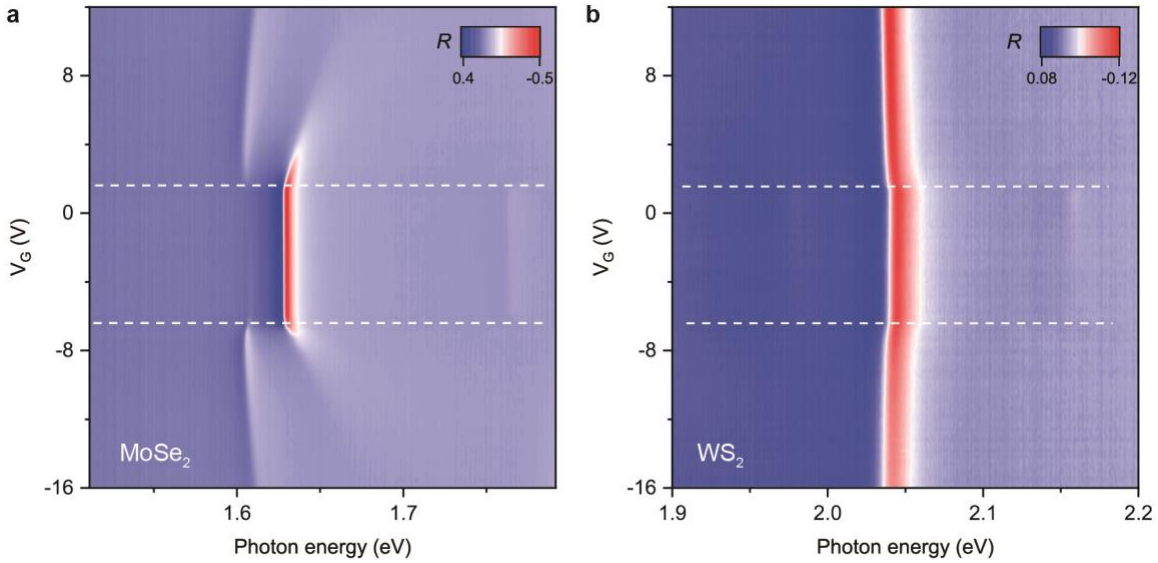

Extended Data Figure 10 | Band alignment in $MoSe_2/WS_2$. a,b, Doping-dependent reflectance contrast spectrum of a 20°-aligned $MoSe_2/WS_2$ bilayer focusing on the fundamental intralayer exciton in $MoSe_2$ (**a**) and WS_2 (**b**). The horizontal dashed lines mark the onset of electron and hole doping. The intralayer exciton in $MoSe_2$ loses oscillator strength and evolves into the red-shifted feature (charged excitons) upon both electron and hole doping, suggesting a type-I band alignment.